Heterogeneous Interseismic Coupling Along the Xianshuihe-Xiaojiang Fault System, Eastern Tibet

Yanchuan Li, Jean-Mathieu Nocquet, Xinjian Shan, Huizi Jian

JGR Solid Earth

RESEARCH ARTICLE
10.1029/2020JB021187

Special Section:
Creep on continental faults and subduction zones: Geophysics, geology, and mechanics

Heterogeneous Interseismic Coupling Along the Xianshuihe-Xiaojiang Fault System, Eastern Tibet

Yanchuan Li[1,2], Jean-Mathieu Nocquet[1,3], Xinjian Shan[2], and Huizi Jian[2]

[1]Geoazur, Université Côte d'Azur, IRD, CNRS, Observatoire de la Côte d'Azur, Valbonne, France, [2]State Key Laboratory of Earthquake Dynamics, Institute of Geology, China Earthquake Administration, Beijing, China, [3]Institut de Physique du Globe de Paris, Université de Paris, Paris, France

Key Points:

- Highly heterogeneous interseismic coupling along the Xianshuihe-Xiaojiang fault system, with the northern Xianshuihe fault predominantly creeping at depth
- Surface creep observed during 4 decades after the 1973 M 7.6 Luhuo earthquake has ended
- A new ~30 km-long transient creeping segment on the Xianshuihe fault, with creep rate increasing after the 2008 Mw 7.9 Wenchuan earthquake

Supporting Information:

Supporting Information may be found in the online version of this article.

Correspondence to:

Y. Li,
yanchuan@ies.ac.cn

Citation:

Li, Y., Nocquet, J.-M., Shan, X., & Jian, H. (2021). Heterogeneous interseismic coupling along the Xianshuihe-Xiaojiang fault system, eastern Tibet. *Journal of Geophysical Research: Solid Earth*, *126*, e2020JB021187. https://doi.org/10.1029/2020JB021187

Received 14 OCT 2020
Accepted 7 OCT 2021

Abstract We use Global Positioning System (GPS) and Interferometric Synthetic Aperture Radar (InSAR) data to quantify the interseismic coupling along the Xianshuihe-Xiaojiang fault system (XXFS). Our results confirm 7–11 mm/a of left-lateral strike-slip motion along the XXFS. South of the Shimian County, high interseismic coupling is found down to 20 km-depth along the Anninghe-Zemuhe fault. A second 130 km-long section, highly coupled down to 10–15 km-depth, is identified along the northern Xiaojiang fault. North of the Kangding County, the Xianshuihe fault appears to be predominantly creeping at depth. Previously identified long-lasting surface creep following the 1973 M 7.6 Luhuo earthquake has now ended, possibly marking the initiation of a new period of stress accumulation and progressive relocking of the fault. Farther south along the fault, we identify a ~30 km-long section (~30.2°–30.4°N) creeping at ~7 mm/yr. Furthermore, creep accelerated by ~2 mm/yr during the 2008–2014 period, possibly as a result of the static Coulomb failure stress increment induced by the 2008 Mw 7.9 Wenchuan earthquake, that occurred ~200 km northeast of it. The 2014 Mw 5.9 Kangding earthquake occurred along the creeping section at the end of the period of accelerated creep. Finally, taking advantage of the long historical records of past large earthquakes available since 1327, we quantitatively compare the moment budget along the XXFS. Results highlight that along the Anninghe, Zemuhe, and Xiaojiang faults, moment deficit for Mw > 7 earthquakes has now accumulated.

Plain Language Summary More probable location and size of future large earthquakes can be anticipated if we accurately know the present-day distribution of interseismic fault coupling. Knowing date of the latest large earthquake, one can infer slip deficit and estimate the energy available for forthcoming seismic ruptures. Here, we focus on the Xianshuihe-Anninghe-Zemuhe-Xiaojiang fault system in Tibet, which is the largest strike-slip fault crossing southwestern China. Historical records attest numerous earthquakes during the last few centuries, but the fault has remained relatively silent in the past few decades. We use GPS data spanning nearly 20 years to investigate the present-day interseismic fault coupling along the fault system. We find the Anninghe, Zemuhe, and Xiaojiang faults have accumulated enough energy for several Mw > 7 earthquakes. However, our results show that the northern segment called the Xianshuihe fault is not locked, suggesting a relatively low energy accumulation rate and seismic potential, despite a long history of frequent earthquakes. Finally, we identify a new ~30 km-long creeping section on the Xianshuihe fault, whose creep rate show a transient behavior, possibly induced by the effect a ~200 km remote earthquake that occurred in 2008.

1. Introduction

The 1400 km-long left-lateral strike-slip Xianshuihe-Anninghe-Zemuhe-Xiaojiang fault system (XXFS) is one of the largest faults cutting through eastern Tibet and contributing its eastward motion (e.g., Allen et al., 1991; Tapponnier et al., 2001; Tapponnier & Molnar, 1977). East of the Tibetan Plateau, the XXFS extends across the Sichuan and Yunnan provinces and merges with the Red River fault (Figure 1). The XXFS has been one of the most seismically active faults in mainland China, as attested by a detailed history of past earthquakes for the last three centuries (e.g., Allen et al., 1991; Wen, Ma, et al., 2008). Indeed, during that period, historical records indicate more than 35 earthquakes with magnitude estimated to be larger than 6. Additional historical records dating back to the XIVth century indicate that each of the four faults has hosted at least one large $M > 7.5$ earthquake and the largest event with an estimated magnitude reaching eight occurred in 1833 along the Xiaojiang fault in Yunnan. According to the earthquake history

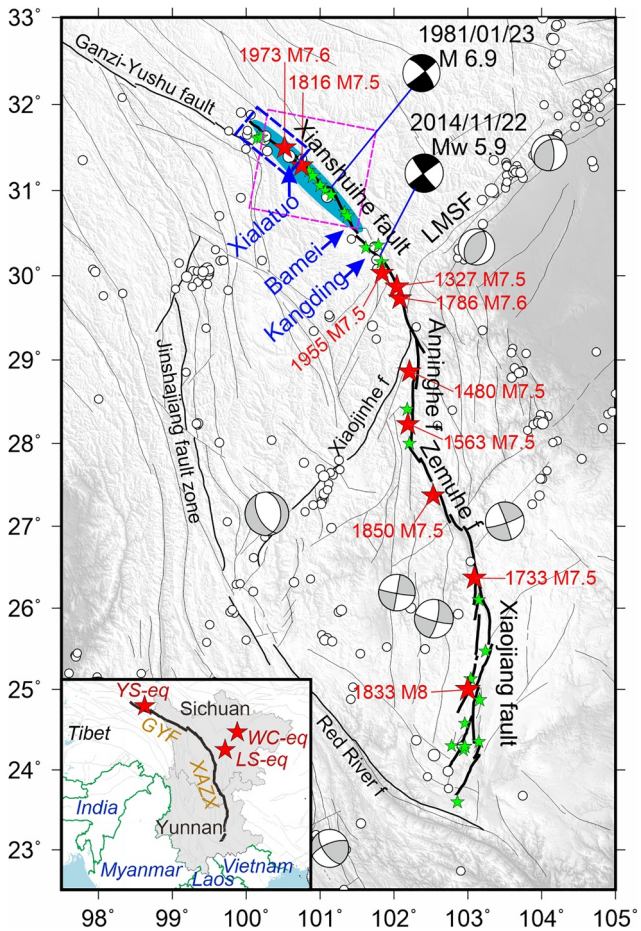

Figure 1. Regional tectonic map of the eastern Tibetan Plateau. Bold black lines correspond to the Xianshuihe-Anninghe-Zemuhe-Xiaojiang fault system (XXFS). Thin black lines indicate others active faults (Deng et al., 2003). Focal mechanism solutions (Mw > 6, 1976–2015) are from the Global Centroid Moment Tensor (GCMT). Thin white circles are earthquakes (Mw > 5, 1960–2015) from the United States Geological Survey (USGS). Red ($M \geq 7.5$) and green ($M > 6$) stars mark the epicenters of historical earthquakes (Wen, Ma, et al., 2008). The pink rectangle shows InSAR data coverage used in this study (see Figure 3). Cyan ellipse indicates creeping sections proposed by Allen et al. (1991) and Zhang, Wen, et al. (2018). The blue rectangle outlines the surface rupture of the 1973 M 7.6 Luhuo earthquake. LMSF denotes the Longmenshan fault. The inset map highlights the Sichuan and Yunnan provinces. Red stars show the locations of 2008 Mw 7.9 Wenchuan earthquake (WC-eq), 2013 Mw 6.5 Lushan earthquake (LS-eq) and 2010 Mw 6.8 Yushu earthquake (YS-eq). GYF denotes the Ganzi-Yushu fault.

summarized by Wen, Ma, et al. (2008), the Xianshuihe fault hosted regular large events with $M > 7.5$ earthquakes in 1327, 1786, 1816, 1955, and 1973 (Figure 1). Despite some large uncertainties in the size and rupture area of past earthquakes that are to be expected from historical data, this high past seismic activity contrasts with the seismic quiescence observed for nearly half a century, with only two moderate earthquakes recorded in 1981 (M 6.9) and 2014 (Mw 5.9) along the northwestern sections.

Several studies have assessed the short-term seismic potential along XXFS. Ran et al. (2008) and Wen, Ma, et al. (2008) show that for the Xianshuihe fault, from the Kangding County to Bamei Town (hereafter refer to the Kangding-Bamei section, Figure 1) and for the Anninghe fault, the time elapsed since the last large earthquake (232 and 528 years respectively) is close to the average earthquake recurrence time (230–350 and 520–660 years respectively) proposed from paleoseismology studies (Allen et al., 1991). Interseismic fault coupling inversions constrained by GPS data in the 1999–2013 period also find that the Kangding-Bamei section and the Anninghe fault have accumulated enough slip deficit for characteristic earthquakes to happen (Mw 7.0 and Mw 7.5 respectively, G. Jiang et al., 2015). Since the region crossed by the XXFS hosts a dense population of more than 50 million inhabitants, assessing the seismic potential of the XXFS is a major issue in a rapidly developing area in China.

The Xianshuihe fault further provides an opportunity to gain insight into faulting behaviors following large earthquakes. From an analysis of short-baseline (~130 m) conventional geodetic survey data (1976–1984), Allen et al. (1991) found up to ~6 mm/a of surface creep at Xialatuo site (100.75°E, 31.28°N. Figure 1) along the 1973 Luhuo earthquake surface rupture. Recently, Zhang, Wen, et al. (2018) reprocessed the short-baseline and short-leveling arrays data (1976–2014) at seven sites along the Xianshuihe fault, and report an average creep rate of 1.3–3.5 mm/a extending 2–7 km depth during the observation span, decaying through time at a logarithmic rate (cyan ellipse in Figure 1 outlines the creeping sections). Oppositely, H. Wang et al. (2009) interpret the fault section between ~31° and 31.8°N along the Xianshuihe fault be locked down to a depth of 3–6 km using ERS-1/2 and Envisat SAR data for the 1996–2008 period. These different results may reflect a progressive relocking of the section ruptured by the 1973 Luhuo earthquake.

In this study, we first derive GPS velocity solutions for the eastern Tibetan Plateau, spanning time periods of 1999–2007, 1999–2014, and 2015–2018, respectively. These time periods are roughly separated by two earthquakes that occurred in eastern Tibet, namely the 2008 Mw 7.9 Wenchuan and 2014 Mw 5.9 Kangding earthquakes. Then, using an elastic block model, we estimate the spatial distribution of interseismic fault coupling (ISC) along the XXFS. Using the available history of past earthquakes, we derive balances of moment accumulation and release and discuss their implications in terms of present-day seismic potential for the main faults of the XXFS. Finally, we identify a ~30 km-long creeping section on the Xianshuihe fault, which does not overlap and is located south of the creep sections described in Allen et al. (1991) and Zhang, Wen, et al. (2018). We investigate the temporal variations in creep rate and its implication for the fault behavior.

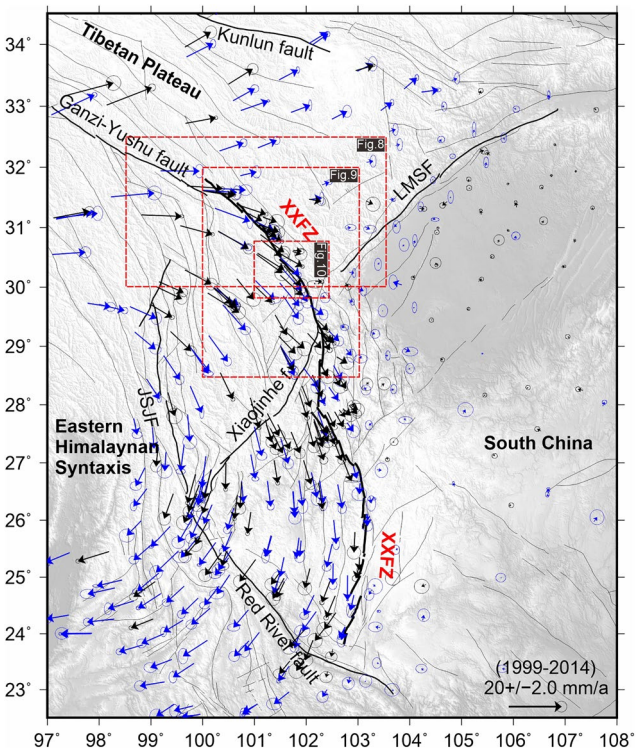

Figure 2. Global Positioning System (GPS) horizontal velocity fields (1999–2014) with respect to the South China block. Arrows in blue represent the velocity solution from Wang, Qiao, et al. (2017). Arrows in black represent the velocity solution from Rui and Stamps (2016). Error ellipses show 68% confidence levels. Thin black lines correspond to active faults. Dotted red rectangles outline the location of Figures 8, 9 and 10. JSJF denotes the Jinshajiang fault.

2. Data and Model

2.1. GPS Data Processing

We use three different GPS velocity solutions, spanning the 1999–2007, 1999–2014, and 2015–2018 periods, to investigate the heterogeneous coupling and temporal variations in the location of creeping sections of the fault.

1. The 1999–2007 GPS velocity solution, which is used in Section 4.2 and 4.3 to detect creep rate variations on the Xianshuihe fault, is from Zhang et al. (2013). This solution is expressed in a Eurasia plate reference frame and represents interseismic velocities for eastern Tibet before the 2008 Mw 7.9 Wenchuan earthquake, but with relatively low spatial resolution.
2. The 1999–2014 GPS velocity solution is used as input for our elastic block model described in Section 2.2.2, whose spatial density is higher than that of previous studies (e.g., G. Jiang et al., 2015; Zheng et al., 2017). It consists of two parts:
   - The Crustal Movement Observation Network of China (CMONOC) GPS data acquired between 1999 and 2014, including a total of 300 sites in the study area (244 campaign and 56 continuous stations). The velocity solution is derived from Wang, Qiao, et al. (2017). During the processing, co-seismic offsets from the 2001 Mw 7.8 Kokoxili, 2004 Mw 9.2 Sumatra, 2008 Mw 7.9 Wenchuan, 2010 Mw 6.8 Yushu and 2011 Mw 9.0 Tohoku earthquakes were removed. For the postseismic perturbations from large earthquakes in eastern Tibet, post-earthquake data of near-field stations were not included. Stations located near the rupture zones with no observations prior to the earthquakes were also excluded.
   - The GNSS/GPS Network of the Sichuan Earthquake Bureau and the Sichuan Surveying and Mapping Bureau, including 177 sites that were occupied between 2004 and 2014. This velocity solution comes from Rui and Stamps (2016). Coseismic displacements at GPS stations were considered as offset parameters during the coordinate time series fitting. For postseismic transients following the 2008 Mw 7.9 Wenchuan earthquake, 9 months of GPS observations after the earthquake were removed during velocity estimate. Similarly, GPS data collected after the 2013 Mw 6.5 Lushan earthquake were excluded. Text S1 in Supporting Information S1 provides details of GPS data processing and data selection.

The two GPS velocity solutions are originally referenced to different realizations of the Eurasia plate reference frame. We combine them into a single consistent solution by solving for an Euler vector, which minimizes the velocity difference at co-located sites, using the solution of Wang, Qiao, et al. (2017) as the reference. The Root Mean Square (RMS) value for the postfit velocity residuals at 197 sites common to both solutions is 0.86 mm/a. Figure S1 in Supporting Information S1 shows the difference of GPS velocities for the 1999–2007 and 1999–2014 solutions at sites common to both solutions. The velocity differences are within their 68% confidence level error ellipses, implying the postseismic deformation induced by the large earthquakes after 2008 does not significantly impact the 1999–2014 GPS velocity solution. To highlight the relative motion between Tibet and South China, Figure 2 shows our final combined velocity field in a South China fixed reference frame.

3. The 2015–2018 GPS velocity solution is also used in Section 4.2 and 4.3 to detect creep rate variations along the Xianshuihe fault. We process the raw data of the CMONOC GPS network following the processing strategies of Li et al. (2018). We obtain the GPS velocity field in eastern Tibet in the International

Terrestrial Reference System 2014 (ITRF2014), and then transform it in a Eurasia plate reference frame using the Euler pole from Altamimi et al. (2017).

In August 8, 2017, a Mw 6.5 earthquake struck the Jiuzhaigou County (epicenter 103.861°E, 33.198°N), ~350 km north away from XXFS. A forward coseismic slip model shows that the spatial extent of coseismic displacement field is less than 150 km from the epicenter (Zhao et al., 2018), we thus correct the coseismic offsets for GPS stations located within the range during data processing. A forward postseismic model shows this earthquake produced ~0–0.4 mm/a deformation at our GPS sites (within 100 km from the epicenter) during the 2017–2018 period (Figure S2 in Supporting Information S1). The velocity differences between the 1999–2007 and 2015–2018 solutions are within their 68% confidence level error ellipses (Figures S1 and S2 in Supporting Information S1), indicating that transient postseismic deformation in eastern Tibet does not impact the velocity estimates in our 2015–2018 solution. GPS time series of several continuous sites (Figure S3 in Supporting Information S1) are shown in Figure S4 in Supporting Information S1.

2.2. GPS Data Modeling

2.2.1. 2-D Modeling

We evaluate fault creep rate at specific locations along XXFS using a buried dislocation model. The 2-D elastic dislocation model (Segall, 2010; Weertman & Weertman, 1964) fits the fault parallel velocities (V_{par}) and solves for a slip rate (S), a locking depth (d_1), and a creep rate (C) from the surface to depth (d_2):

$$V_{\mathrm{par}}\left(x\right) = \frac{S}{\pi}\tan^{-1}\left[\frac{x}{d_1}\right] + \frac{C}{\pi}\tan^{-1}\left[\frac{d_2}{x}\right] + a \tag{1}$$

where a is a constant and x is the distance from the fault.

We use a Bayesian approach to derive posterior probability density functions (PDF) of the model parameters (Minson et al., 2013; Nocquet, 2018), which is defined as $p\left(\boldsymbol{m}|\boldsymbol{d}\right) \sim p\left(\boldsymbol{m}\right)\exp\left[\left(\boldsymbol{d}-\boldsymbol{r}\right)^T C^{-1}\left(\boldsymbol{d}-\boldsymbol{r}\right)\right]$, where $\boldsymbol{d}$ and $\boldsymbol{r}$ are vectors containing the observations and model predictions, C^{-1} is the data covariance matrix (here simply taken as a diagonal matrix), and $p(\boldsymbol{m})$ is the prior PDF of the model parameters, taken as uniform distributions. Results (mean values) described in Section 4.2 and 4.3 are derived from a total of 50,000 sampling from a Markov chain implemented in the PyMC Python package (Patil et al., 2010). Parameter uncertainties are derived from the posterior distribution of models.

2.2.2. 3-D Modeling

We use the elastic block modeling implemented in the DEFNODE package (McCaffrey et al., 2007) to obtain a regional kinematic model (Section 3). We simultaneously solve for block rotation rates, strain rates within blocks, and spatially variable distribution of interseismic coupling along block-bounding faults.

With reference to previous studies (e.g., Loveless & Meade, 2011; Wang, Qiao, et al., 2017), the southeastern Tibetan Plateau is divided into five tectonic blocks (Figure S5 in Supporting Information S1). The Songpan-Ganzi domain is divided into the Longmenshan and Bayanha sub-blocks (Loveless & Meade, 2011), and the Sichuan-Yunnan terrace is divided into the North Yunnan and South Yunnan sub-blocks (Wang, Qiao, et al., 2017). The Xianshuihe fault forms the boundary between Longmenshan and North Yunnan blocks, and the Anninghe-Zemuhe-Xiaojiang faults separate the South Yunnan block from the South China block (G. Jiang et al., 2015). The South China block is assumed to be rigid and we solve for internal strains within the other blocks. A few studies further divide the South China block into two sub-blocks (e.g., Y. Wang et al., 2008, Wang, Qiao, Yang & Wang, 2017), where the Daliangshan fault acts as their boundary. We do not include the sub-block for two reasons. First, compared with the Anninghe and Zemuhe faults, the Daliangshan fault is significantly less seismically active (e.g., Sun et al., 2019). Second, if the Daliangshan fault is included in block model, despite the RMS value of GPS velocity residuals decreases from 1.60 mm/a to 1.52 mm/a, this decrease is found to be statistically not significant given the increased number of free parameters. Besides, the estimated slip rate along the Daliangshan

fault can reach ~6–7 mm/a, a value much larger than the ~2–5 mm/a slip rate on the Anninghe-Zemuhe fault in the same model (e.g., Y. Wang et al., 2008). Such results are at odd with the earthquake history (Wen, Ma, et al., 2008).

In the model, faults are represented by a set of 3-D nodes (distance of 30 km along-strike and 5 km along-dip) defining the fault plane and the ISC at each node is estimated during the inversion. We impose an along-strike smoothing constraint on the ISC values by keeping their along-strike change below a specified value. For example, a smoothing constraint of 0.5 permits a variation in ISC of 0.5 or less over a 1° distance (~111 km) along strike, while a very low smoothing value (<0.1) will produce an extremely smooth model. Given the relatively dense distribution of GPS sites in eastern Tibet (average spacing of ~30 km around the XXFS), we adopt a smoothing parameter of 1.0 to allow large variations in ISC over wavelengths shorter than ~111 km. We do not impose any along dip constraint to avoid oversmoothed results that might mask potential surface creep along the XXFS.

The fault interface between nodes is divided into patches of 10 km along strike and 1.7 km along dip. A bi-linear interpolation is applied to obtain the ISC for each patch. We model the XXFS as a 80° southwestward dipping fault, consistent with previous studies (e.g., Allen et al., 1991; Deng et al., 2003; G. Jiang et al., 2015; Wen, Ma, et al., 2008). The Longmenshan fault is modeled to be listric in shape (Thompson et al., 2015), while the remaining block-bounding faults are taken vertical. The Bamei-Kangding section, which consists of two strands, namely the Yalahe and Selaha faults, is modeled as one strand. This simplification is justified by the fact that the two faults merge into a single fault at depth, the former of which slips at 1.0 ± 0.5 mm/a and accounts only ~10% of the total slip along the Xianshuihe fault (e.g., Chen et al., 2008).

In order to account for the elastic contribution of locked faults surrounding the XXFS, we first solve for a uniform fault locking depth for all of the block-bounding faults using a grid search method (between 2 and 30 km with a step of 2 km). Results (Figure S6a in Supporting Information S1) show GPS data could not distinguish models with fault locking depth in 20–30 km. Besides, variations of locking depth for block-bounding faults, except for the XXFS, do not affect much the inversion results (Figure S6b in Supporting Information S1). Nonetheless, we find that 95% of the micro-seismicity in eastern Tibet occurs within the first 20 km (Figure S6b in Supporting Information S1). Therefore, a uniform fault locking depth of 20 km (consistent with that of Wang, Wang, & Shen, 2017) is used for the block-bounding faults. ISCs along the XXFS are parameters to be estimated in the inversion.

The optimal model is obtained by minimizing data misfit defined by the reduced chi-squared statistic (χ_n^2):

$$\chi_n^2 = \Sigma_1^n \left(\frac{\gamma_i}{\sigma_i} \right)^2 / \left(n - m \right) \tag{2}$$

where n is the number of observations, m is the number of free parameters, γ_i is the residuals (observed minus calculated velocities), and σ_i is the data uncertainty for observation .

2.2.3. Resolution Test

Three kinds of resolution tests are conducted to investigate the robustness of our estimates of the fault coupling and moment deficit rate. Figure S7 in Supporting Information S1 shows the GPS sites used in the tests.

First, we calculate the sensitivity of the model to the GPS data set, using the model resolution matrix defined as $\mathbf{S} = \mathrm{diag}(\mathbf{G}^t\mathbf{G})$, where $\mathbf{G}$ is the matrix of the elastic Green function used in the interseismic backslip calculation (e.g., Loveless & Meade, 2011), and diag is the vector of diagonal elements. Every row in $\mathbf{S}$ corresponds to a model parameter m_i and the values (defined as Resolution, R) in the row describe how well the ith parameter is solved by data. When the only nonzero value is 1, the corresponding parameter m_i is perfectly solved, otherwise the data can solve only a weighted combination of parameters (Menke, 1989). To investigate the sensitivity of GPS sites to coupling variations along strike and dip, we calculate the resolution by increasing size of individual elements (along-strike patch sizes from 20 to 70 km, along-dip patch size of 5 km). Results (Figure S8 in Supporting Information S1) indicate that, in case of along-strike patch size of 30 km, the dense GPS sites can constrain well ($R \geq 0.5$) the ISC for the upper 10–15 km of the Xianshuihe,

Anninghe, and Zemuhe faults. Despite relatively poor resolution along the central Xiaojiang fault due to sparser data, a critical value of resolution $R = 0.1$ is reached. As expected, as the size of the patch increases, the resolution increases, but at the risk of missing details in spatial coupling variations along strike.

Second, we run several forward models (along-strike patch sizes from 20 to 70 km, along-dip patch size of 10 km) with starting coupling values with either 1 or 0, then add random errors with the same variance as those of the observed GPS velocity solution to the forward velocities, and finally invert the fault coupling along the XXFS. Results (Figure S9 in Supporting Information S1) show that lateral variations of 30 km are recovered above a depth of ~10–15 km from the Xianshuihe fault to Zemuhe fault, whereas a depth of ~10 km along the central section of the Xiaojiang fault. This result is consistent with the above resolution calculation.

Third, we investigate whether the moment deficit rates could be biased as the locking depth increases. Results from our test (Figure S10 in Supporting Information S1) show that moment deficit rates are consistently retrieved when asperities are locked down to 10–15 km. Underestimation by ~6% arises when the asperity is locked at 20 km. We therefore assign a 10% uncertainty in moment budget calculations described in Section 4.1.

We conclude from the above tests that the distribution of GPS stations allows sensitivity to coupling variations over a distance larger than 30 km along strike and within 10–15 km depth on the XXFS, whereas coupling below 15 km represents an averaged locking state. Because they use integral of slip deficit rate over the fault plane, seismic moment balances as described in Section 4.1 are not significantly biased when the maximum locking depth of the fault is changed.

2.3. InSAR Data and Reprocessing

We compile interseismic InSAR Line-of-Sight (LOS) rate (data span: December 2014 to November 2016, Figure 3a) from Zhang, Cao, et al. (2018) covering the Xianshuihe fault between ~30.5° and 31.6°N. They used the ROI_PAC software for the raw data processing. Topographic phase bias was removed using a simulated phase from the 1-arc Digital Elevation Model. Atmospheric and elevation correction were conducted using the standard Small Baselines Subset chain (Berardino et al., 2002).

We adopt the remove-filter-restore approach proposed by Wei et al. (2010) to make GPS (1999–2014) and InSAR data mutually consistent for subsequent modeling. The method assumes that GPS-derived velocity field is dominated by the long wavelength horizontal crustal deformation, while the InSAR-derived LOS rate field is composed of both the long and short wavelength 3-D information. In Wei et al.'s approach, the first step is to remove the GPS-interpolated horizontal velocity (projected onto LOS) from LOS, then high-pass filter the LOS residuals using a Gaussian filter, and finally add the high-pass filtered results back to the GPS velocity map (interpolation expressed in LOS), referred as the restored InSAR. The restored InSAR (Figure 3b) preserves the short wavelength features of InSAR and long wavelength features of GPS, allowing us to derive the "surface creep rates" along the Xianshuihe fault (Section 4.2). The "surface creep rate" is calculated as the difference in fault-parallel velocity averaged in 1 km normal and 2 km along the strike bins on opposite sides of the fault (e.g., Li et al., 2021). If the fault segment is creeping, the "creep rate" should be significantly larger than the uncertainty.

3. Interseismic Coupling Results

We obtain the angular velocities and internal strain parameters of each block, and ISCs along the block bounding faults in our best fitting model. The angular velocities are used to calculate the slip rate along the XXFS (Figure 4). The XXFS is dominated by left-lateral strike-slip motion with the fastest rates of 10–11 mm/a found along the northwesternmost section of the Xianshuihe fault, progressively decreasing to 7 mm/a along the Anninghe, Zemuhe and Xiaojiang faults. These estimates are consistent with both geological (~9–10 mm/a; e.g., Bai et al., 2018; Yan & Lin, 2017) and previous geodetic results (~7–13 mm/a; e.g., Loveless & Meade, 2011; Shen et al., 2005; Wang, Qiao, et al., 2017). Small fault-perpendicular rates of 0.2–2.1 mm/a (shortening) and 0–1.3 mm/a (extension) are found along the Xianshuihe-Anninghe fault and Zemuhe-Xiaojiang fault respectively.

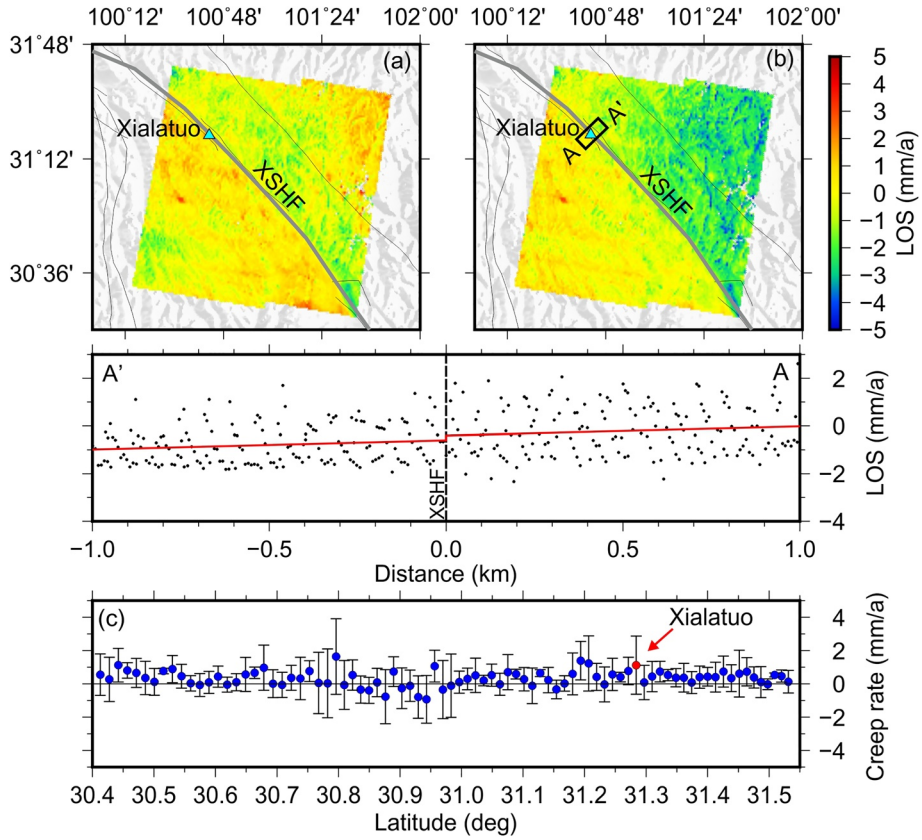

Figure 3. (a) InSAR LOS rate map across the Xianshuihe fault from Zhang, Cao, et al. (2018). (b) The restored InSAR LOS rate map across the Xianshuihe fault (see text for details). Black rectangles show the locations of the velocity profile across the fault at the Xialatuo site, with the associated Line-of-Sight (LOS) velocities below. Red lines are best linear fits of the data each side of the fault. (c) Along fault variations of creep rates for the Xianshuihe fault derived from the InSAR data. The blue error bars are 1-σ uncertainties.

Our ISC model highlights two opposite behaviors. From latitude 32°N to latitude 30°N, the Xianshuihe fault appears to be predominantly creeping, while the Anninghe, Zemuhe, and Xiaojiang faults show significant coupling. In the detail, high coupling occurs along three locked regions hereafter referred as A1 (~24.3°–24.6°N, A being an abbreviation for asperity), A2 (~24.9°–26.6°N), and A3 (~26.8°–29.7°N), separated by narrow sections of shallower (~5 km depth) or weaker coupling (Figure 4). A1 located along the southernmost part of the Xiaojiang fault appears to be locked down to ~20 km depth. However, since this location corresponds to the edge of the model, we cannot rule out the possibility of boundary effects and we do not interpret this pattern in the following discussion. A2 along the Xiaojiang fault is confined to ~10 km depth but spans ~130 km along strike. The largest A3 is found to be locked down to ~20 km and extends laterally over ~240 km along the Anninghe and Zemuhe faults. According to our resolution and checkerboard tests (Figures S8 and S9 in Supporting Information S1), variations in slip rate deficit on A2 and A3 could be resolved by our GPS data, and seismic moment balances calculated on these asperities as described in Section 4.1 would not significantly biased.

Additional remarkable features of the fault coupling are the shallow locking depth found along several sections (hereafter refer to S1, S2, S3, and S4, S is an abbreviation for Section. Figure 4). S1, located along the northwestern section of the Xianshuihe fault between latitude 30.4° to 32°N, shows a very shallow averaged locking depth of 2–3 km. S1 overlaps the section experiencing surface creep found by Allen et al. (1991) and Zhang, Wen, et al. (2018). Adjacent to S1, the S2 section extends ~30 km along the Xianshuihe fault between latitude 30.2° to 30.4°N and overlaps the Kangding-Bamei section. ISCs along S2 are estimated to be smaller than 20%, possibly reflecting creep reaching the surface. From our block model, the surface creep rate is estimated to be ~7.5 mm/a, comparable with the estimated long-term slip rate from the relative block motion

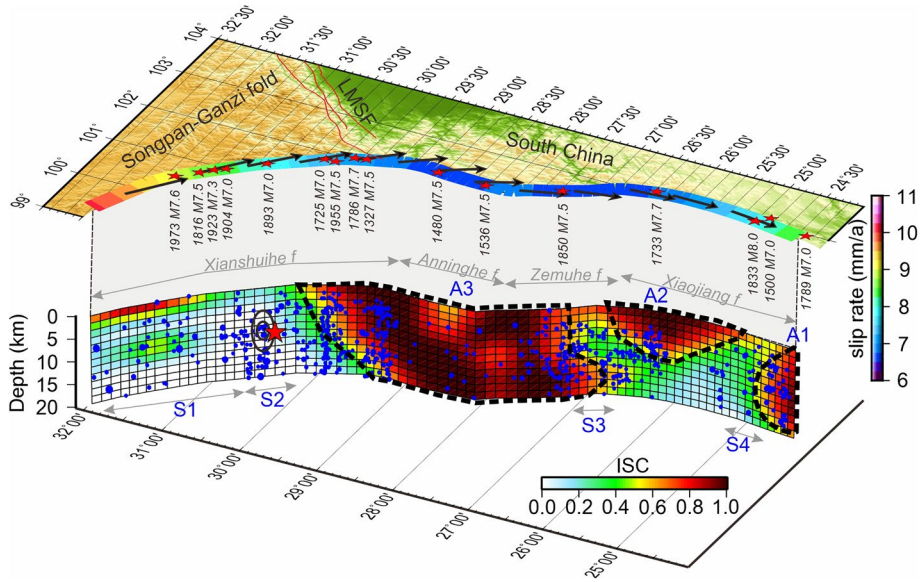

Figure 4. Modeled fault slip rate and interseismic fault coupling (ISC) along the Xianshuihe-Anninghe-Zemuhe-Xiaojiang fault system (XXFS). Upper panel: Fault slip rate along the XXFS. Fault slip rate magnitude is color coded according to the upper-right color scale, black arrows indicate fault slip direction. Red stars denote locations of historical earthquakes. Lower panel: ISC distribution along the XXFS plane. Blue dots indicate hypocenters of microseismicity (1970–2015, China Earthquake Data Center, http://data.earthquake.cn. See Supplementary data). Thick black dotted lines outline highly locked areas, labeled as A1, A2, and A3. The red star shows the hypocenter of the 2014 Mw 5.9 Kangding earthquake, and the black ellipses outline the 0.2 and 0.4 m coseismic slip contours from Jiang et al. (2015).

(7.9 ± 1.6 mm/a). S3 (~26.6°–26.8°N) and S4 (~24.6°–24.9°N) are short sections separating the locked asperities A2–A3 and A1–A2 respectively, with averaged fault locking depths in the range of ~2–5 km.

We show the block internal strain rates and GPS residuals in Figure S5 in Supporting Information S1. Tables S1 and S2 in Supporting Information S1 list block rotation and strain rate parameters. The principal strain rates are 7.4–0.04, 3.3–8.0, 1.0–3.9, and 2.4–10.1 (compressive–tensile in nanostrain per year) for the South Yunnan, North Yunnan, Longmenshan, and Bayanha blocks respectively. These strain rate values highlight submillimeter per year internal deformation at the scale of the blocks in eastern Tibet.

4. Discussion

Our results show highly heterogeneous fault locking along the XXFS (Figure 4). Taking benefit from the relatively complete history of past earthquakes along the XXFS, we use our ISC results to quantitatively calculate the moment budget along different fault sections and infer areas with the highest amount of accumulated moment, hence prone to a higher probability of future seismic ruptures.

Because the time elapsed since the last large earthquake is different along the different sections of the XXFS, our ISC results also provide an opportunity to explore the fault behavior at different stages of the earthquake cycle. Specifically, we discuss the shallow creep detected along the Xianshuihe fault in the context of the sequence of past earthquakes, and evaluate the temporal variations in creep rate.

4.1. Fault Behavior and Moment Budget Along the XXFS

4.1.1. Overall Characteristics

We first evaluate the overall consistency or differences between our fault coupling model and the results from previous studies. Our results highlight four sections (S1, S2, S3, and S4) with low fault locking and two highly locked potentially seismogenic asperities (A2 and A3) (Figure 4). Although consistent with previous results at the first order (G. Jiang et al., 2015), our current GPS data set has a better spatial resolution and

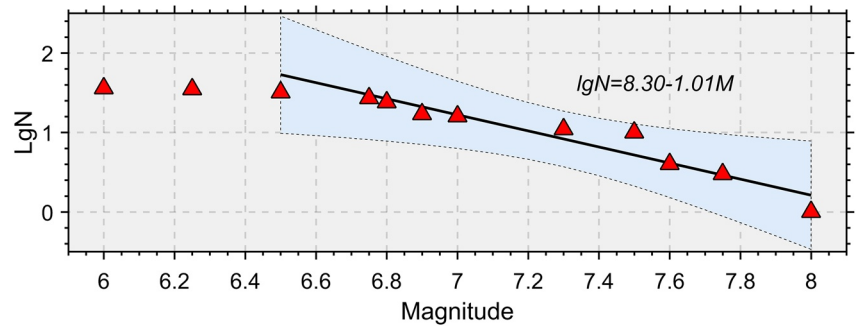

Figure 5. Gutenberg-Richter law showing the relation between the frequency and magnitude for known earthquakes during the 1327–2018 period along the XXFS. Black line represents the best linear fit for earthquakes with magnitudes larger than 6.5. Light-blue background shows 95% confidence level of the linear fit.

identifies a new creeping section (30.2°–30.4°N, S2) along the Xianshuihe fault. As an external verification, Figure 4 shows the fault coupling together with the background seismicity. Earthquakes from the China Earthquake Data Center catalog are selected within a 15 km wide swath (approximate the uncertainty level of earthquake location, C. Jiang et al., 2008) along the XXFS, spanning a period from January 1970 to November 2014 (Figure S11 in Supporting Information S1). Apart from S2, possibly biased by the aftershocks of the 2014 Mw 5.9 Kangding earthquake, most of the micro-seismicity appears to occur at the transition zones between locked and creeping sections. Such observation is similar to other faults like the Himalayan thrust for instance (Stevens & Avouac, 2015) and consistent with the view that increased shear stress occurs as a result of slip gradient on the fault plane.

The earthquake history available for the XXFS allows us to quantitatively assess the seismic moment budget over time along the different sections of the XXFS. Such calculations rely on the completeness and reliability of the historical earthquake catalog. The long history of written records in the densely populated Sichuan and Yunnan regions makes it unlikely that any major earthquake ($M > 7$) would have been left unrecorded. In order to further test the reliability of the earthquake catalog derived from Wen, Ma, et al. (2008), we calculate the frequency-magnitude plot of earthquakes for the whole XXFS for the period 1327–2018. A least squares fit of a Gutenberg-Richter (Gutenberg & Richter, 1944) distribution of earthquakes shows a *b*-value of 1.01, suggesting that the earthquake catalog is complete for earthquakes with magnitude larger than 6.5 (Figure 5). For a maximum magnitude close to 8, neglecting all $M < 6.5$ earthquakes would bias the seismic moment budget by 17%, and by only ~10% if half of them were missing. Owing to their limited contribution to the moment release compared to $M > 7$ earthquakes, they do not affect significantly the moment budget presented below. In the following, we use a division of main fault sections guided by our coupling inversion, fault geometries and historical large earthquakes (Figures 4 and 6).

4.1.2. Northern Xianshuihe Fault

The ISC result shows significant lateral variations along the Xianshuihe fault (Figure 4). We divide the Xianshuihe fault into 2 sub-sections Sa1 & Sa2 (Figure 6). Sa1 is located north of the Bamei Town and encompasses the shallowly locked section S1 (Figure 4). Sa2 from Bamei Town to Shimian County, encompasses the creeping section S2 and part of A3 (Figure 4).

Along Sa1, at least 12 earthquakes with magnitude larger than 6 occurred during the past 300 years (Figure 6). The present-day averaged fault locking depth of 2–3 km indicates that the fault is predominantly creeping at depth and is at odd with the earthquake history. Sa1 has been last ruptured in 1893 (M 7) for the southern part, in 1923 (M 7.3) and 1981 (M 6.9) for the central part and in 1967 (M 6.8) and 1973 (M 7.6) for the northern part. For the northern section, shallow creep has been observed from short baseline geodetic measurements since 1976 (Allen et al., 1991; Zhang, Wen, et al., 2018). Figure 7a shows the measurements of surface creep rate following the 1973 M 7.6 Luhuo earthquake. Surface creep lasted more than 4 decades after the earthquake, with a logarithmic decay of its rate through time, indicating a progressive relocking of the fault at shallow depth. Maximum creep rate is observed along the southern part of the 1973 earthquake rupture (3.5 mm/a in 1976–2014) and to a lesser extent in its northern part (1.3 mm/a), whereas the central

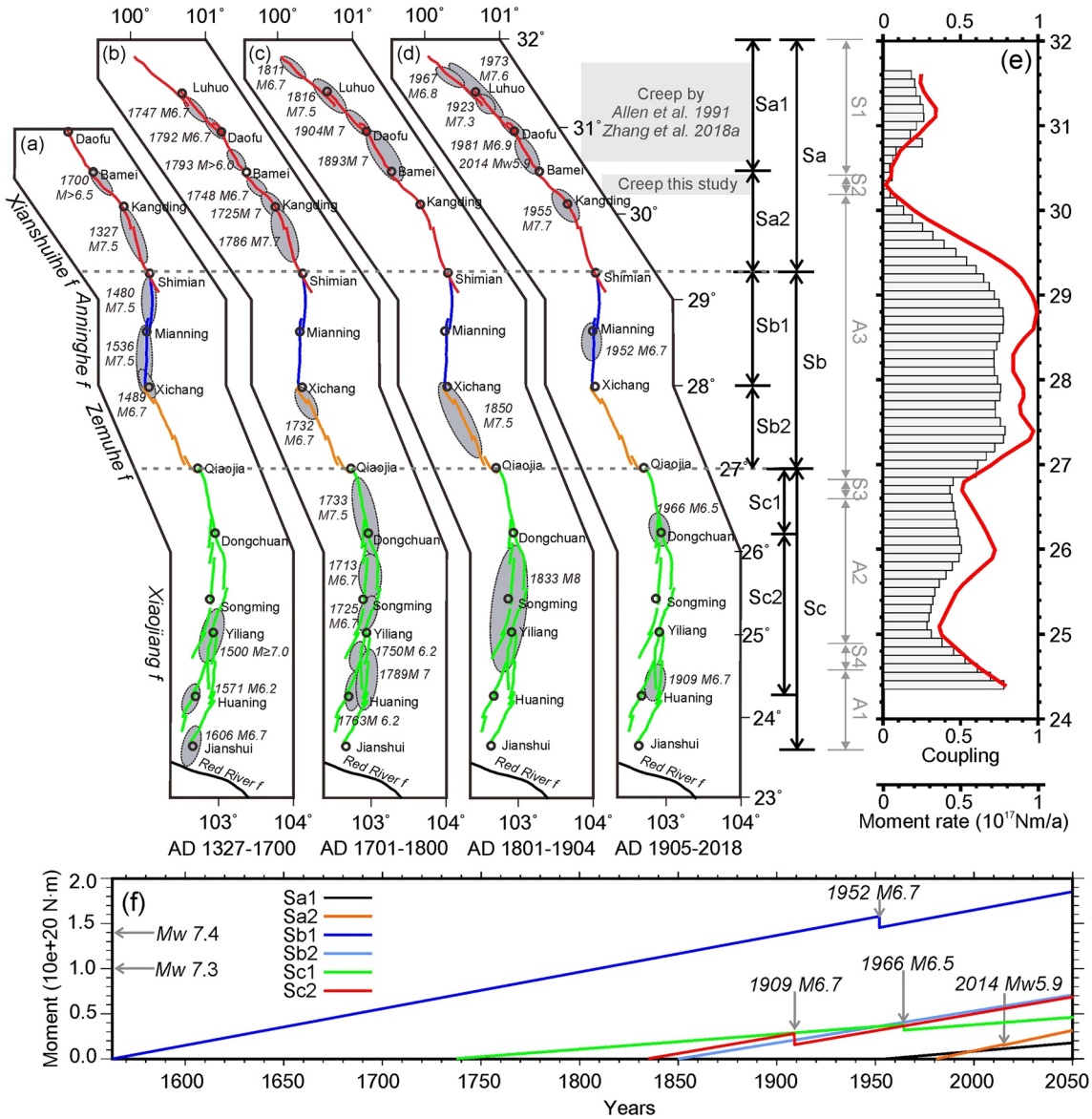

Figure 6. (a–d) Maps for four historical periods of damaged areas for 36 $M \geq 6$ earthquakes along the XXFS (modified from Wen, Ma, et al., 2008). Gray ellipses show the damaged areas for every earthquake together with the earthquake date and magnitude proposed by Wen, Ma, et al. (2008). The red, blue, yellow and green lines correspond to the Xianshuihe fault, the Anninghe fault, the Zemuhe fault and the Xiaojiang fault respectively. (e) The red line corresponds to the vertically averaged coupling coefficients above 10 km depth. Gray histograms represent cumulative seismic moments every 0.2° bin between 0 and 20 km depth. (f) Moment deficit accumulation and released through earthquake as a function of time since 1536, for the 6 segments of the XXFS labeled in (a–d).

part experienced little if any aseismic motion (Figure 7b). Surface creep is also observed in the southern part of the 1923 rupture section after the 1981 M 6.9 earthquake. Along the 1893 earthquake rupture trace, short-baseline measurements do not show significant surface creep. Nonetheless, our ISC model finds a still weak coupling with an average coupling coefficient of ~20%–40% in that area (Figures 4 and 6e).

We compare the rate of moment accumulation predicted by our model with the seismic moment released by past large earthquakes. Taking a 10% uncertainty in the geodetic estimates (see Section 2.2.3) and using an elastic shear modulus of 30 GPa, our model indicates a rate of moment deficit accumulation of 4.21–5.15 × 10^{17} N m/a. The amount of moment released by earthquakes since 1700 is 7.26 × 10^{20} N m (Figure 6), corresponding to ~1410–1724 years of moment accumulated at the present-day rate with no earthquakes. Even considering that the magnitudes of historical earthquake are overestimated by 0.2, the resulting time span would be ~708–867 years. There is clearly a discrepancy here, which originates from

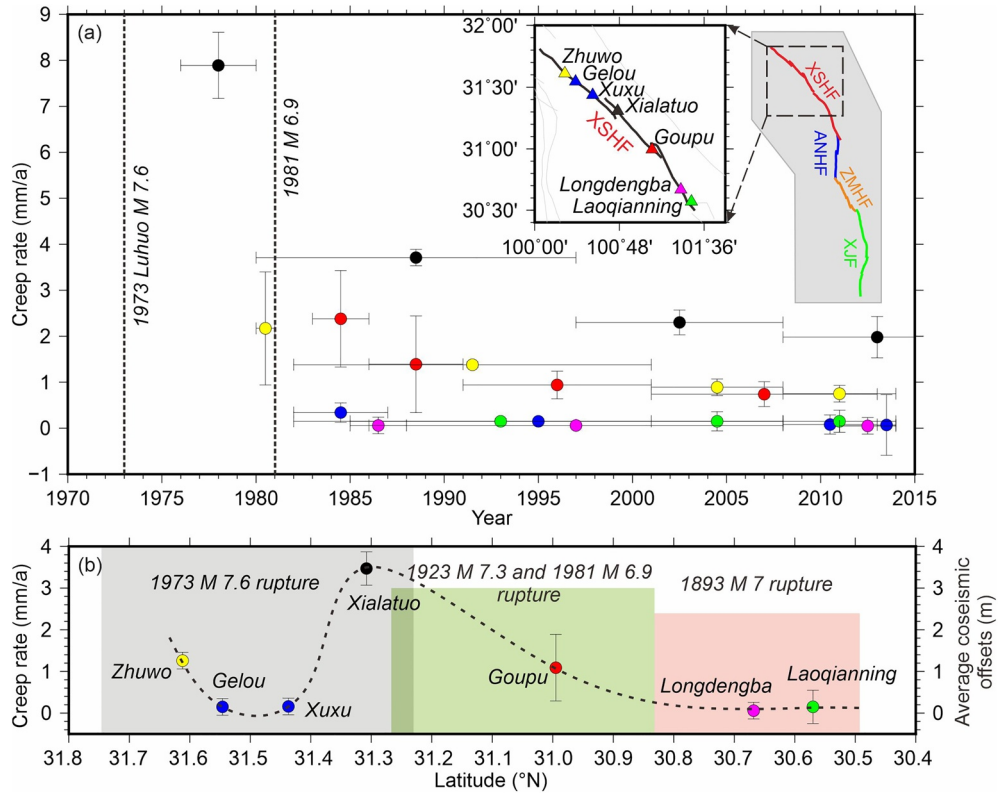

Figure 7. (a) Surface creep rate derived from short baseline measurements as a function of time along the Xianshuihe fault. Dot color show the measurements at different sites, whose location and color code are shown in the inset. Vertical dotted lines represent the date of the 1973 M 7.6 and 1981 M 6.9 earthquakes. For clarity, vertical error bars show 3-σ uncertainty, while horizontal error bar show the period used to estimate the surface creep rate. (b) Colored dots show the average surface creep rate (left vertical axis) at 7 measurement sites along the Xianshuihe fault during the whole observation period. Error bars show 3-σ uncertainty associated to the creep rates. Dotted line indicates the overall shape of the creep distribution along the Xianshuihe fault. Background color corresponds to the average surface offset (right vertical axis) of each earthquake (Papadimitriou et al., 2004).

either an abnormally high frequency of earthquakes during the last three centuries or a too weak amount of present-day accumulation moment rate that would then not be representative of the longer-term average fault coupling. The above comparison ignores the strain released by potential postseismic creep following large earthquakes. If considered, it would further support our speculation. As a point of comparison, if we assume the 205 km-long fault to be entirely locked down to 15–20 km depth, a moment accumulation rate of 9.23–12.3 × 10^{17} N m/a (10 mm/a × 15–20 km × 205 km × 30 GPa) leads to a moment deficit of 6.03–8.04 × 10^{20} N m over the 1327–1981 period, a value roughly consistent with the moment released by earthquakes over the same period.

Together with the transient creep from short baseline geodesy, this calculation supports the view that at the scale of several centuries, the northern Xianshuihe fault is locked and that the current behavior represents a transient behavior, progressively moving toward a relocking of the fault and perhaps initiating a new cycle. Similar "supercycles," that are periods of abnormally high frequency of large earthquakes separated by periods of quiesence has been documented for several faults (e.g., Nocquet et al., 2017; Sieh et al., 2008).

This result raises several questions. First, afterslip here appears to be long lasting compared to previous results, which usually indicate decay-time of a few years (e.g., Hsu et al., 2002). Here, accelerated surface creep lasted several decades after the 1973 and 1981 earthquakes and our ISC model indicates that no significant locking even for the section ruptured in 1893. The Xianshuihe case of long-lasting afterslip might not be so uncommon however. For instance, the afterslip following the 2004 Mw 6.0 Parkfield strike-slip earthquake lasted ~6–12 years (e.g., Lienkaemper & McFarland, 2017). The 1944 (Mw 7.2) and 1951 (Mw

6.9) strike-slip earthquakes along the North Anatolian Fault generated afterslip continuing during at least 20 years, probably up to 50–70 year, along the Ismetpasa segment, which is still creeping nowadays (e.g., Bilham et al., 2016; Cakir et al., 2005; Cetin et al., 2014; Ozener et al., 2013; Rousset et al., 2016). Second, although the lack of coseismic slip models for previous earthquakes and the resolution of our model both prevent to document the spatial relationship between rupture and long lasting afterslip, our result indicates that on average from 20 km depth to the surface, the fault is freely slipping. This certainly encompasses areas that were locked before the earthquake and were involved during the rupture of past large earthquakes. So, the observation here suggests that progressive slow relocking is taking place and ruptured area did not relock immediately after the seismic rupture. Lasting several decades, this slow process of progressive relocking is not short with respect to the average recurrence time between successive earthquakes.

4.1.3. Southern Xianshuihe Fault

Along Sa2, our ISC result shows two opposite behaviors, with almost full decoupling (locking coefficient of <20%) along the Bamei-Kangding section (i.e., S2 in Figure 4), and a transition toward full coupling down to ~10–20 km depth along the Kangding-Shimian section (Figures 4 and 6e). Our results show discrepancies with previous results from G. Jiang et al. (2015), who used a viscoelastic model and reported 60%–100% locking along the Bamei-Kangding section, and a shallow fault locking depth of 0–10 km along the Kangding-Shimian section. The discrepancies might be attributed to different models and data sets. Our checkerboard tests indicate a fairly good resolution along this section (Figures S8 and S9 in Supporting Information S1).

We present in paragraph 4.2 additional results for the Bamei-Kanding section showing that this section is also currently experiencing surface creep. South of it, the Kangding-Shimian section hosted an M 7.7 earthquake in 1955. Unlike the Sa1 section, the Kangding-Shimian marks a transition from mild coupling (locking coefficient of 0.2 at Kangding) to tight coupling (locking coefficient of 0.9 at Shimian). In addition to the 1955 M 7.7 earthquake, this section also experienced large earthquakes in 1327 (M 7.5) and 1786 (M 7.7, Figure 6). Such magnitudes are consistent with a full rupture of its 165 km length (Mw 7.67), according to the earthquake scaling relationships (Cheng et al., 2019; Wells & Coppersmith, 1994). This allows to test whether the moment released in earthquakes over 7 centuries is consistent with the present-day geodetically derived moment accumulation model. Our model provides an accumulation rate of moment deficit at $1.68–2.06 \times 10^{17}$ N m/a, equivalent to a total moment of $1.06–1.29 \times 10^{20}$ N m between 1327 and 1955. This amount is less than 15% of the released moment through coseismic ruptures (8.41×10^{20} N m) during the same period. Now considering that this fault section is 100% coupled down to 15–20 km, the accumulation rate of moment deficit is $5.57–7.43 \times 10^{17}$ N m/a, resulting in a moment of $3.50–4.66 \times 10^{20}$ N m for the 1327–1955 period. Such values are 70%–90% of the moment release in coseismic ruptures. Nevertheless, given that there may be uncertainties in qualifying the magnitude of historical earthquakes (Wen, Ma, et al., 2008), the strain balance can be considered as being achieved to the first order.

This result suggests that the present-day rate of moment deficit accumulation is also somehow transient along this section. More specifically, the newly creeping section identified here along the Bamei-Kanding section is probably also a transient feature. We further show in Section 4.2 that it underwent creep rate variations at the time scale of a few years. Combining the results for both Sa1 & Sa2 sections, the Xianshuihe fault appears to be in a transient state following a rich sequence of earthquakes for the last three centuries, and then initiating a new cycle of progressive increasing locking. Overall, given the past sequence of earthquakes and the still low present-day rate of moment deficit accumulation, the seismic potential appears weaker than for the other sections of the XXFS. For the area from Kangding to Shimian, if we assume the 1955 M 7.7 to have released all the previously accumulated elastic strain along that section, our coupling model finds that the current moment available for an earthquake is Mw 6.7.

4.1.4. Anninghe-Zemuhe Fault

The Anninghe-Zemuhe fault involves the main coupled part of the XXFS (A3 in Figure 4), where full locking down to ~20 km-depth along a 240 km-long section is obtained from our block model (Figures 4 and 6e). The history of earthquakes shows that the northern section from Shimian to Xichang Towns did not experience any large earthquake for more than four centuries (last $M > 7$ earthquake occurred in 1563), while the southern section last ruptured in 1850. A slip deficit of 2–4 m is thus expected along the Anninghe-Zemuhe

fault, corresponding to high potential of a large earthquake, a result consistent with the seismic gap proposed by Wen, Fan, et al. (2008).

The northern section (Sb1) has a length of 150-km and is able to host a Mw 7.6 earthquake according to fault-length magnitude scaling laws (Cheng et al., 2019; Wells & Coppersmith, 1994). For the moment balance calculation here, we assume that the 1536 M 7.5 earthquake released all the accumulated moment for this section. Under this assumption, we find a geodetic total moment deficit of 1.88–2.30 $\times 10^{20}$ N·m in the 1536–2050 period at an accumulation rate of 3.65–4.47 $\times 10^{17}$ N m/a from our block model. This amount is equivalent to a Mw 7.5 earthquake if all the accumulated moment would be released in a single event (Figure 6f).

Along the southern section Sb2, the 130 km-long section is capable of rupture in a Mw 7.5 earthquake. We thus consider that the 1850 M 7.5 earthquake as our starting date for the moment balance assessment. Our model predicts a moment deficit accumulation rate of 3.19–3.89 $\times 10^{17}$ N m/a. By 2050, this amount leads to a moment of 6.38–7.78 $\times 10^{19}$ N m which can be balanced by a Mw 7.2 earthquake (Figure 6f).

Overall, the Anninghe-Zemuhe fault shows a much larger seismic potential than the Xianshuihe fault.

4.1.5. Xiaojiang Fault

The southern part of the XXFS fault shows along strike varying coupling, with a ~180 km-long highly locked section (A2 in Figure 4), surrounded by sections with shallow locking depth (S3 and S4 in Figure 4). High locking close to the southern tip of the XXFS is also imaged by our model but with a lower resolution due to possible side effects at the merging of the Xiaojiang fault with the Red River fault (A1 in Figure 4).

From the past history of earthquakes dating back to the XVIth century, we do not observe a clear segmentation of earthquakes with the one suggested by our ISC models. Indeed, S3 and S4 were at least partially ruptured in the 1733 M 7.5 and 1833 M 8 earthquakes respectively. Given the time elapsed since these earthquakes, shallow locking here probably reflects lateral frictional variations along the Xiaojiang fault rather than transient creep following large earthquakes.

Here, accumulated moment along the 90-km-long fault section between Qiaojia-Dongchuan (Sc1) equals to an Mw 7.1 earthquake in the 1733–2050 period. We assume that the 1833 M 8 earthquake released all elastic strain along the 180-km-long section from Dongchuan to Huaning (Sc2). At the estimated moment deficit rate from our ISC model, we find an equivalent single event of Mw 7.2 is required by 2050 to balance the accumulated moment since 1833 (Figure 6f).

4.1.6. Summary of Seismic Potential Along XXFS

According to earthquake rupture length-magnitude scaling relationship (Cheng et al., 2019; Wells & Coppersmith, 1994), the empirical maximum magnitudes of earthquakes are Mw 7.6 and Mw 7.5 along the Anninghe fault (Sb1, 150 km-long) and the Zemuhe fault (Sb2, 130 km-long), respectively. The accumulated moment from our coupling model (Figure 6f) and the above empirical calculation suggest that the Anninghe and Zemuhe faults are ready for large earthquakes in the next decades, as already pointed out by several studies (e.g., G. Jiang et al., 2015; Ran et al., 2008; Wen, Ma, et al., 2008). Besides, we find that the Xiaojiang fault has a relatively high seismic potential with accumulated moment deficit allowing for Mw > 7 earthquakes to happen.

Along the Kangding-Bamei section (~30.0°–30.5°N), paleoseismological studies (e.g., Ran et al., 2008; Wen, Ma, et al., 2008) indicate that the time elapsed since the last large earthquake (232 years) is close to the average earthquake recurrence time (230–350 years). Previous interseismic fault coupling results constrained by GPS data suggest this section has accumulated enough slip deficit for a Mw 7 earthquake (e.g., G. Jiang et al., 2015). However, our block model results indicate that this section has very shallow locking depths (0–5 km), and includes a creeping section (S2 in Figure 4) between latitude ~30.2°–30.4°N. Relatively low moment accumulation rate and magnitude of accumulated slip deficit suggest that earthquake potential might have been overestimated by previous studies along this part of the fault system.

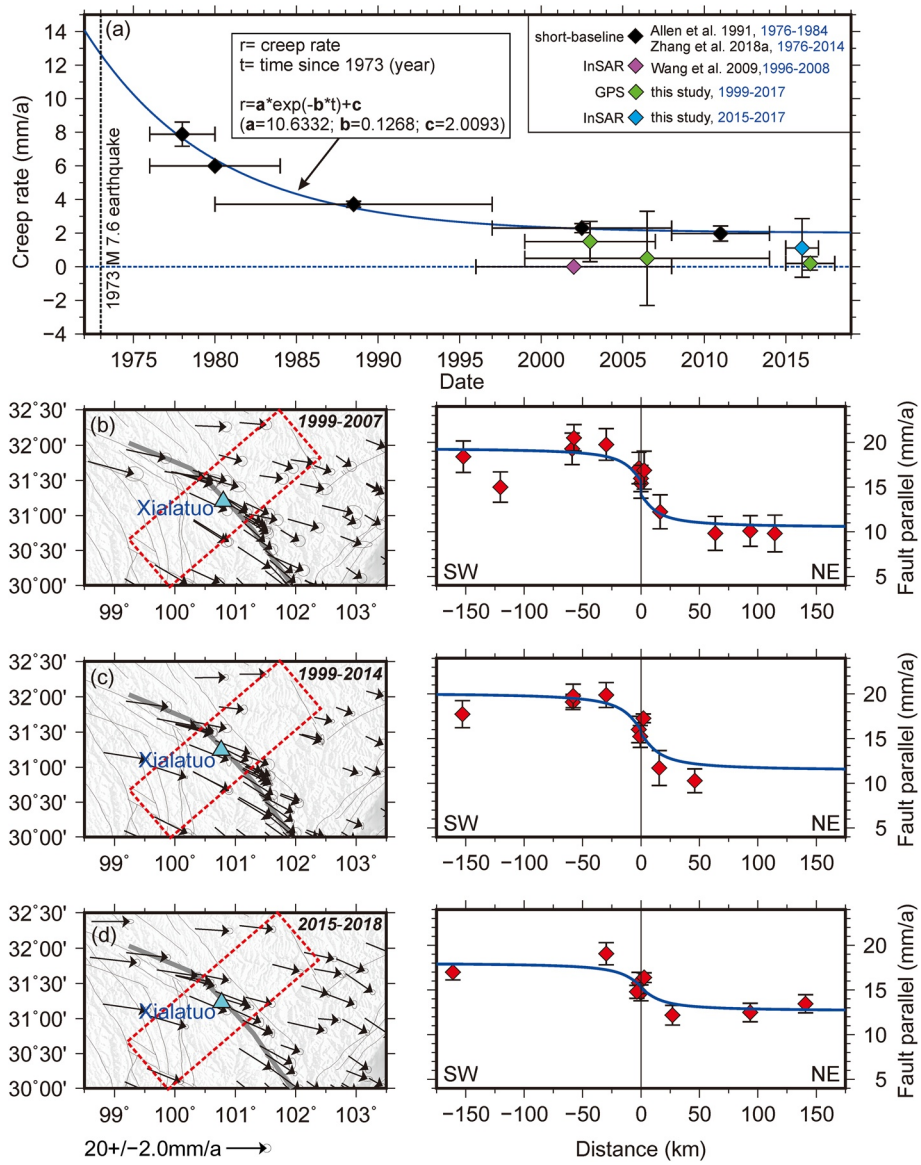

Figure 8. (a) Fault creep rate at the Xialatuo site as a function of time. Blue solid line is the best decreasing exponential fit of short-baseline measurements. Vertical error bars show 1-σ uncertainty, horizontal error bars show the time period used for each measurement. (b) GPS velocity solution (Eurasia fixed reference frame, error ellipses at 68% confidence levels) in 1999–2007 and corresponding fault parallel velocities across the Xialatuo site (error bars show 1-σ uncertainty), with its locations shown in red rectangles in the left panel. Blue solid line represents the best fitting curve. (c) and (d) are GPS velocity solutions (Eurasia fixed reference frame) for the 1999–2014 and 2015–2018 periods respectively. Fault normal components are show in Figure S12 in Supporting Information S1, and PDFs of estimated fault parameters are shown in Figure S13 in Supporting Information S1.

4.2. Shallow Creep Along the Xianshuihe Fault

The above moment budget calculations along the Xianshuihe fault suggest that the shallow creep documented along several sections of the fault is transient at the scale of the earthquake cycle. Here, we focus on shorter time scale variation of the creep. Zhang, Wen, et al. (2018) collected and processed the short-baseline and short-leveling data (1976–2014) measured at seven sites along the Xianshuihe fault (Figure 7a). They propose that spatio-temporal variations in surface creep rates occur between latitudes ~30.5° and 31.6°N. In Figure 8a, we summarize the estimates of creep rate at Xialatuo site and fit a decreasing exponential function as a function of time (Cakir et al., 2005). For comparison, estimates from our GPS study

and InSAR analysis are shown but are not used in the exponential function fitting. The creep rate shows an exponentially decay with time from ~8 mm/a in 1976–1980 to ~2 mm/a or less in 2008–2014. Extrapolated to the date of the 1973 Lushuo earthquake, the surface creep rate would be 12 mm/a, slightly exceeding the loading rate (~8.7 mm/a) due to the relative block motion across the Xianshuihe fault.

Modern geodesy observations, to some extent, show discrepancies with repeated short-baseline measurements results for the latest period (Zhang, Wen, et al., 2018). For instance, Qiao and Zhou (2021) and Li and Bürgmann (2021) suggest the fault section between ~31.0° and 31.8°N along the Xianshuihe fault creeps at ~2.5–3.5 mm/a in the 2014–2019 period. H. Wang et al. (2009) report that this section was locked down to a depth of 3–6 km by processing SAR data acquired in 1996–2008. Our block model also finds a shallow locking depth (2–3 km) along this fault section (Figure 4). To provide another independent observation of shallow creep along this section, we fit a simple 2-D elastic dislocation model (Section 2.2.1) to the fault parallel GPS velocities across the fault at the Xialatuo site (Figures 8b–8d, fault normal components are show in Figure S12 in Supporting Information S1). The curve fit provides a creep rate estimate of 1.5 ± 1.2 mm/a for the 1999–2007 period, 0.5 ± 2.8 mm/a for the 1999–2014 and 0.2 ± 0.4 mm/a for the 2015–2018 period (PDFs of estimated parameters are shown in Figure S13 in Supporting Information S1). These results suggest that creep at Xialatuo sites ended during the 2000–2018 period. To further investigate if there is any creep signal along the Xianshuihe fault between ~30.5° and ~31.6°N, we use the InSAR data (2014–2016, Figure 3b) across the fault and estimate "creep rates" (see Section 2.3). The result (Figures 3c and 8a) also shows no apparent creep signal. Space geodetic creep results (0–1.5 mm/a) are smaller than those obtained from ground short-baseline measurements results (2–3 mm/a, Zhang, Wen, et al., 2018) for the 1996–2018 period. The creep rate discrepancy might be due to either different datasets or different period used to calculate it. As predicted by the exponential function (Figure 8a), the average creep rate in 1996–2008 is ~2 mm/a, which is approximately the precision level of geodetic observations (i.e., GPS and InSAR), making difficult to detect it. Alternatively, the surface creep following the 1973 M 7.6 Luhuo earthquake might have ended before 1996. The creeping results derived from short-baseline measurements (1996–2014) are limited by their spatial coverage (baseline length <300 m), thus the observations are probably related to a shattered or damaged fault zone in the shallow sediments (e.g., Hamiel et al., 2018). Such interpretation implies that the Xianshuihe fault experienced postseismic deformation in a period (before 1996) shorter than the 41+ years (1973–2014+) proposed by Zhang, Wen, et al. (2018). Despite these subtle differences between our results and Zhang, Wen, et al. (2018), both studies show that the shallow creep section along the Xianshuihe fault (~30.5°–31.6°N) is at present in a state of progressive relocking of the shallow part of the fault, initiating of a new cycle of stress accumulation.

The other creep section highlighted by our GPS results lies in ~30.2°–30.4°N along the Bamei-Kangding section, which extends ~30 km-long (Figure 4). To provide independent reference for the existence of creep section as well as the creep rate, we also fit 2-D elastic dislocation model to the fault parallel GPS velocities (Figure 9a show profiles location and fit of our best model, fault normal components are show in Figure S14 in Supporting Information S1). Results show sharp but continuously gradient across the fault for AA' and CC' north and south of the creeping section, indicating locked fault sections with locking depths of 5.9 ± 2.1 km and 7.1 ± 4.3 km respectively. The estimated values (within 95% confidence interval) overlap with the 2–3 km fault locking depth from our block model. However, for profile BB' crossing our proposed creep section, GPS velocities show apparent offset across the fault, indicating surface creep. The creep rate is estimated to be 9.0 ± 2.0 mm/a (PDFs are shown in Figure S15 in Supporting Information S1). This surface creep rate is larger than the result from the block model (~7.5 mm/a) but similar to the estimated far-field loading rate (8.8 ± 1.0 mm/a).

One issue here is whether the shallow creep (~30.2°–30.4°N) is a permanent feature or a transient one, with time-decaying rate as found for the northwestern Xianshuihe fault. Paleoseismological investigations identified 17 $M \geq 6.0$ earthquakes along the Xianshuihe fault during the past 700 years (Figures 4 and 6), 16 of which terminated on either side of the creeping section. Only the 1748 M 6.7 earthquake appears to rupture across the identified creeping section. Such medium size earthquake is unlikely to produce afterslip 270 years after its occurrence. The above evidence suggests the fault creep is possibly a permanent feature. Modern microseismicity show cluster beneath the creeping section, indicating the slip deficit on this section is likely released by ruptures of medium-small-sized asperities, and the 1748 M 6.7 earthquake might be

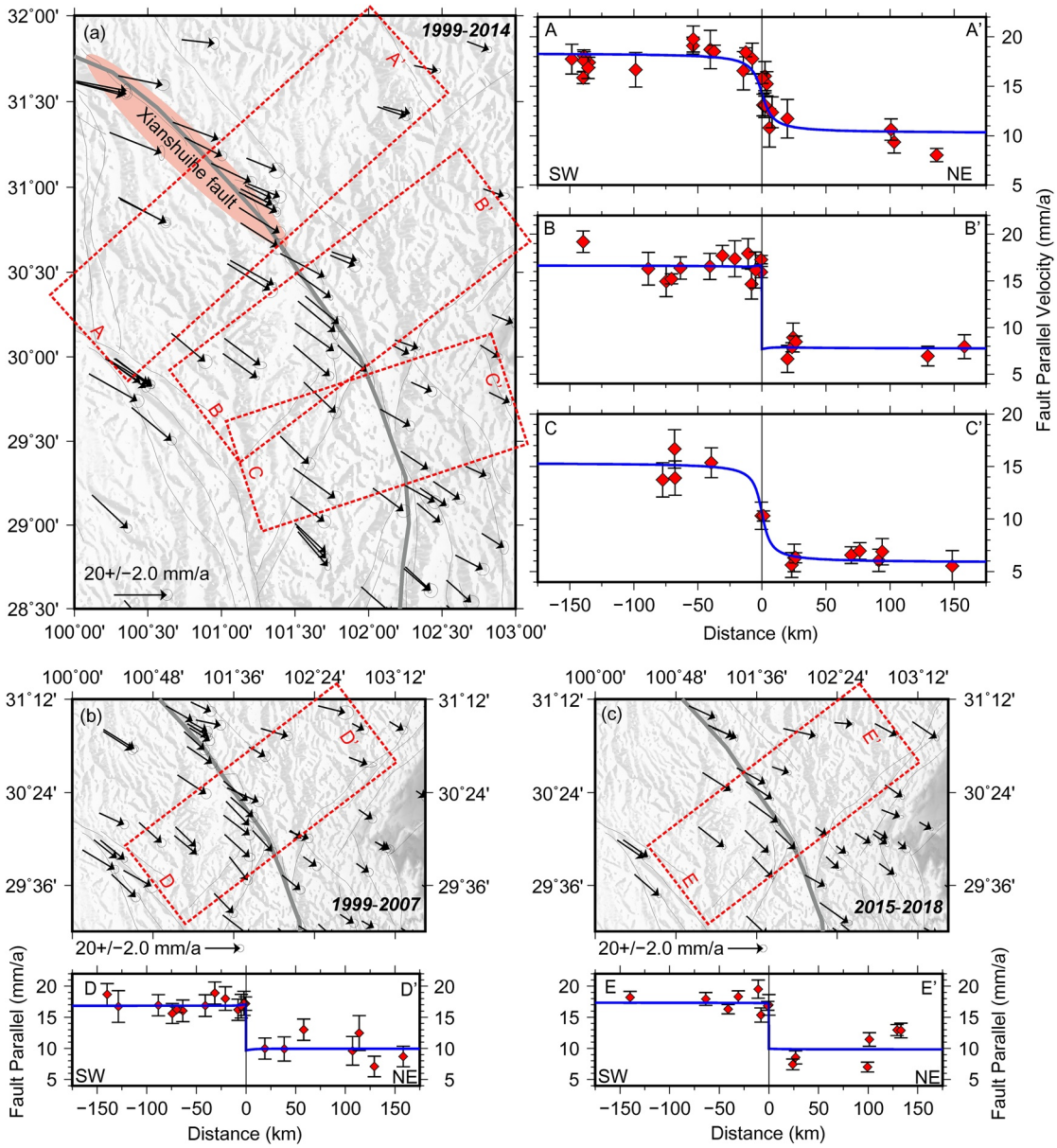

Figure 9. (a) (Left panel) Enlarged map of GPS velocity fields (1998–2014, Eurasia fixed reference frame, error ellipses at the 68% confidence levels) across the Xianshuihe fault. The orange ellipse indicates the creeping sections proposed by Allen et al. (1991) and Zhang, Wen, et al. (2018). (Right panel) Observed and calculated fault-parallel velocities across the Xianshuihe fault, with its locations shown in red rectangles in the left panel. Red diamonds with 1-σ uncertainty error bars show the fault-parallel velocity components of GPS data. Blue curves show prediction for the best fit of 2-D elastic interseismic models. (b) Enlarged map of GPS velocity fields (1999–2007, Eurasia fixed reference frame) across the Xianshuihe fault. Observed and best 2-D interseismic model prediction. (c) Same as (b) for the 2015–2018 GPS velocity field. Fault normal components are show in Figure S14 in Supporting Information S1, PDFs of estimated fault parameters are shown in Figure S15 in Supporting Information S1.

such a case. The November 22, 2014 Mw 5.9 Kangding earthquake ruptured on the part slightly north of the creeping section at 10 km depth (Figure 4). Consequently, it is likely that the creep section has acted as a barrier to the propagation of rupture during earthquakes.

Current observational evidence cannot rule out the possibility that shallow creep on this section has been activated as a propagation of the afterslip along the northwestern Xianshuihe fault. Such inference requires observational evidences at least prior to the 1981 M 6.9 earthquake, we will try to collect available data in our future work.

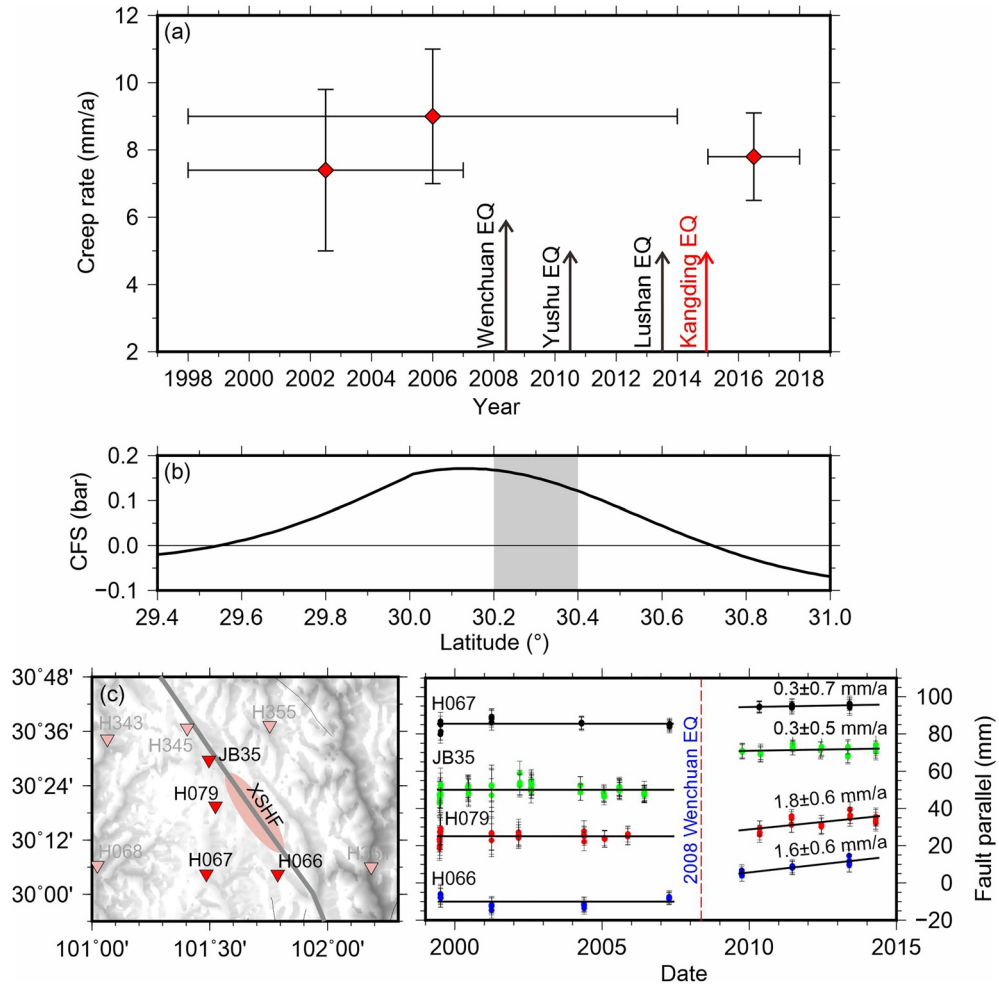

Figure 10. (a) Creep rate along the Xianshuihe fault as a function of time. Error bars show 1-σ uncertainty. Black (red) arrows show the date of large earthquakes in eastern Tibet. (b) Coulomb failure stress changes (ΔCFS) on the Xianshuihe caused by the 2008 Mw 7.9 Wenchuan and the 2013 Mw 6.5 Lushan earthquakes using the model from Shan et al. (2013). Gray rectangle outlines the extent of the creep section found in this study. (c) GPS sites distribution along the Xianshuihe fault. The orange ellipse indicates the proposed creep section. Right panel shows time series of the GPS fault parallel component for the 2009–2015 period with respect to the 1999–2007 taken as reference. Black lines indicate the best linear fit to the data. The red dotted vertical line shows the date of the 2008 Wenchuan earthquake. Note position of the data points along the *y*-axis have been shifted for clarity.

4.3. Temporal Variation in Creep Rate Along the Xianshuihe Fault (~30.2°–30.4°N)

We further investigate if temporal variation in surface creep rate along the Xianshuihe fault (~30.2°–30.4°N) could be detected in our data set. We first fit a 2-D elastic dislocation model to the fault parallel GPS velocities (1999–2007, Figure 9b and Figure S14 in Supporting Information S1) and find a creep rate of 7.4 ± 2.4 mm/a, smaller than the averaged creep rate (9.0 ± 2.0 mm/a) during the 1999–2014 period (Figures 9a and 10a) but consistent with the ~7.5 mm/a estimation by our block model. This comparison in turn implies that the creep rate during the 2008–2014 period should be larger than 9.0 mm/a. We also fit the fault parallel GPS velocities between 2015 and 2018 (Figure 9c and Figure S14 in Supporting Information S1). For this period, the result shows an average creep rate of 7.3 ± 1.5 mm/a, which is similar to that in 1999–2007. The above results therefore indicate an increase in creep rate for the 2008–2014 period, hence implying the creep experienced a pulse (Figure 10a). To provide independent evidence for the temporal variations in creep rate, we finally fit linear constant velocities for four GPS sites that observed in 1999–2015 and that are adjacent to the creep section in different time bin (Figure 10c). For each GPS site, we fit two lines to the time series data, that is, the period in 1999–2007 and 2009–2014. The velocity estimates for the 1999–2007

period is taken as the reference velocity. The results show a slight velocity acceleration (2009–2014) in the fault parallel direction, especially for sites H066 and H079, which are ~8 km from the fault. Moreover, time series of H067 and JB35 (~220 km away from the Wenchuan earthquake surface rupture) show almost indistinguishable velocity changes after the 2008 Mw 7.9 Wenchuan earthquake, suggesting that the velocity variations of the H066 and H079 sites is not induced by the postseismic transients of the Wenchuan earthquake. This further strengthens our inference that the observed velocity acceleration is most likely related to an acceleration of shallow creep. Unfortunately, the few GPS campaign epochs could not provide further constraints on the full time dependent behavior of creep.

We attribute the temporal variation in creep rate to stress perturbations from nearby large earthquakes, that is, the 2008 Mw 7.9 Wenchuan earthquake and the 2013 Mw 6.5 Lushan earthquake (Figure 1), which occurred in eastern Tibet between 2008 and 2014 and overlapped in time with the period of creep acceleration. The coseismic static Coulomb failure stress changes (ΔCFS) and viscoelastic stress changes induced by those earthquakes, mostly induced by the Wenchuan earthquake, are derived from Shan et al. (2013). Text S2 in Supporting Information S1 provides details about our Coulomb failure stress calculation. Positive ΔCFS increases stress loading in certain regions and amplifies the background seismicity, whereas negative ΔCFS could unload the stress on faults and suppress the background seismicity. Figure 10b shows obvious positive CFS of the order of 0.2 bars along the creep section (~30.2°–30.4°N), suggesting that the stress change may have triggered enhanced creep rate along the Xianshuihe fault.

The November 22, 2014 Mw 5.9 Kangding earthquake occurred at a fault portion located slightly north of the creeping section, after the period of creep acceleration. Although the relationship between the earthquake and creep on the Xianshuihe fault remains to be understood, there have been evidences on other continental faults that shallow fault creep rate acceleration could trigger medium-small earthquakes, such as along the Haiyuan fault (e.g., Jolivet et al., 2012). Moreover, by comparing the coseismic slip of the 2014 Mw 5.9 Kangding earthquake with our preferred fault coupling result (Figure 4), we notice that the earthquake ruptured at least part of creep regions, although data resolution does not allow us to better constrain the creep distribution at depth.

5. Conclusions

In this study, we present a detailed description of the crustal deformation along the XXFS, which is one of the most seismically active and potentially most damaging one in China. First, using the GPS velocity solution (1999–2014) for eastern Tibet and the elastic block model, we obtain left-lateral slip rates of 7–11 mm/a along the fault system. In the northern part of the XXFS from 32°N to 30°N, the Xianshuihe fault appears to be predominantly creeping at depth, whereas the Anninghe, Zemuhe and Xiaojiang faults show significant coupling.

The previously reported shallow creep along the northern Xianshuihe fault appears to be long-lasting afterslip following the large (M 7.6 in 1973) and moderate-size (M 6.9 in 1981) earthquakes. Several arguments indicate that relatively weak coupling along the southern Xianshuihe fault is related to past earthquakes in 1955 and even 1893. This is further supported by surface creep along the fault, whose rate decays through time and has possibly ended, therefore initiating a new cycle of increasing slip deficit accumulation.

We further identify that the Kangding-Bamei section includes a ~30 km-long creeping section (30.2°–30.4°N) and find that creep rate accelerated during the 2008–2014 period, likely as a result of stress increments induced by surrounding large earthquakes, the 2008 Mw 7.9 Wenchuan earthquake being the main one. Finally, quantitative calculations of moment budget highlight relatively high seismic potential on the Anninghe, Zemuhe and Xiaojiang faults, where the elastic strain deficit could be balanced by Mw 7.5, Mw 7.2, and Mw 7.1–7.2 earthquakes respectively.

Data Availability Statement

GPS velocity solution of 1999–2007 was derived from Zhang et al. (2013). GPS velocity solution of 1999–2014 was derived from Rui and Stamps (2016) and Wang, Qiao, et al. (2017). GPS velocity solution of 2015–2018 was derived from our own processing of CMONOC GPS data. The GPS time series data (1999–2015)

in Figure 10c were provided by GNSS Data Product Service Platform of China Earthquake Administration. InSAR data came from Zhang, Cao, et al. (2018). GPS velocity solutions, GPS time-series data, fault locking result, background earthquakes (in Figure 4), and GPS profiles data (in Figures 8 and 9) are uploaded at https://osf.io/bhyus/. The authors used the DEFNODE program shared by Robert McCaffrey for the elastic block modeling. Figures were generated using the Generic Mapping Tools (GMT) software (Wessel et al., 2013).

Acknowledgments
The authors are grateful to all colleagues who constructed the GPS network and collected GPS measurements. The authors thank Guoyan Jiang for kindly sharing the coseismic slip result of the 2014 Mw 5.9 Kangding earthquake. The authors show our thanks to Bin Shan for sharing the Coulomb failure stress result on the Xianshuihe fault, to Lei Zhang for sharing the InSAR result. The authors thank Yann Klinger, Romain Jolivet, Cecile Lassere, and Philippe Vernant for helpful comments on earlier version of this manuscript. The authors thank Editors Emma Hill and Yehuda Ben-Zion, and two anonymous reviewers for their thorough and constructive reviews, which greatly improved the quality of this manuscript. This work was supported by the National Key Research and Development Project of China (grant number 2019YFC1509205) and the National Natural Science Foundation of China (grant number 41631073). Yanchuan Li was financially supported by the China Scholarship Council and the China Earthquake Administration.

References

Allen, C. R., Zhuoli, L., Hong, Q., Xueze, W., Huawei, Z., & Weishi, H. (1991). Field study of a highly active fault zone: The Xianshuihe fault of southwestern China. *The Geological Society of America Bulletin*, *103*(9), 1178–1199. https://doi.org/10.1130/0016-7606(1991)103<1178:fsoaha>2.3.co;2

Altamimi, Z., Métivier, L., Rebischung, P., Rouby, H., & Collilieux, X. (2017). ITRF2014 plate motion model. *Geophysical Journal International*, *209*(3), 1906–1912. https://doi.org/10.1093/gji/ggx136

Bai, M., Chevalier, M. L., Pan, J., Replumaz, A., Leloup, P. H., Métois, M., & Li, H. (2018). Southeastward increase of the late Quaternary slip-rate of the Xianshuihe fault, eastern Tibet: Geodynamic and seismic hazard implications. *Earth and Planetary Science Letters*, *485*, 19–31. https://doi.org/10.1016/j.epsl.2017.12.045

Berardino, P., Fornaro, G., Lanari, R., & Sansosti, E. (2002). A new algorithm for surface deformation monitoring based on small baseline differential SAR interferograms. *IEEE Transactions on geoscience and remote sensing*, *40*(11), 2375–2383. https://doi.org/10.1109/tgrs.2002.803792

Bilham, R., Ozener, H., Mencin, D., Dogru, A., Ergintav, S., Cakir, Z., et al. (2016). Surface creep on the North Anatolian fault at Ismetpasa, Turkey, 1944–2016. *Journal of Geophysical Research: Solid Earth*, *121*(10), 7409–7431. https://doi.org/10.1002/2016jb013394

Cakir, Z., Akoglu, A. M., Belabbes, S., Ergintav, S., & Meghraoui, M. (2005). Creeping along the Ismetpasa section of the North Anatolian fault (Western Turkey): Rate and extent from InSAR. *Earth and Planetary Science Letters*, *238*(1–2), 225–234. https://doi.org/10.1016/j.epsl.2005.06.044

Cetin, E., Cakir, Z., Meghraoui, M., Ergintav, S., & Akoglu, A. M. (2014). Extent and distribution of aseismic slip on the Ismetpaşa segment of the North Anatolian Fault (Turkey) from Persistent Scatterer InSAR. *Geochemistry, Geophysics, Geosystems*, *15*(7), 2883–2894. https://doi.org/10.1002/2014gc005307

Chen, G., Xu, X., Wen, X., & Wang, Y. (2008). Kinematical transformation and slip partitioning of northern to eastern active boundary belt of Sichuan-Yunnan block. *Seismology and Geology*, *30*, 58–85.

Cheng, J., Rong, Y., Magistrale, H., Chen, G., & Xu, X. (2019). Earthquake Rupture Scaling Relations for Mainland China. *Seismological Research Letters*, *91*(1), 248–261. https://doi.org/10.1785/0220190129

Deng, Q., Zhang, P., Ran, Y., Yang, X., Min, W., & Chu, Q. (2003). Basic characteristics of active tectonics of China. *Science in China, Series D: Earth Sciences*, *46*, 356–372. https://doi.org/10.1360/03ys9030

Gutenberg, B., & Richter, C. F. (1944). Frequency of earthquakes in California. *Bulletin of the Seismological Society of America*, *34*(4), 185–188. https://doi.org/10.1785/bssa0340040185

Hamiel, Y., Piatibratova, O., Mizrahi, Y., Nahmias, Y., & Sagy, A. (2018). Crustal deformation across the Jericho Valley section of the Dead Sea fault as resolved by detailed field and geodetic observations. *Geophysical Research Letters*, *45*(7), 3043–3050. https://doi.org/10.1002/2018gl077547

Hsu, Y.-J., Bechor, N., Segall, P., Yu, S.-B., Kuo, L.-C., & Ma, K.-F. (2002). Rapid afterslip following the 1999 Chi-Chi, Taiwan Earthquake. *Geophysical Research Letters*, *29*(16), 1–4. https://doi.org/10.1029/2002gl014967

Jiang, C., Wu, Z., & Li, Y. (2008). Estimating the location accuracy of the Beijing Capital Digital Seismograph Network using repeating events. *Chinese Journal of Geophysics*, *51*(3), 817–827.

Jiang, G., Xu, X., Chen, G., Liu, Y., Fukahata, Y., Wang, H., et al. (2015). Geodetic imaging of potential seismogenic asperities on the Xianshuihe-Anninghe-Zemuhe fault system, southwest China, with a new 3-D viscoelastic interseismic coupling model. *Journal of Geophysical Research: Solid Earth*, *120*(3), 1855–1873. https://doi.org/10.1002/2014jb011492

Jolivet, R., Lasserre, C., Doin, M. P., Guillaso, S., Peltzer, G., Dailu, R., et al. (2012). Shallow creep on the Haiyuan fault (Gansu, China) revealed by SAR interferometry. *Journal of Geophysical Research*, *117*, B06401. https://doi.org/10.1029/2011jb008732

Li, Y., & Bürgmann, R. (2021). Partial coupling and earthquake potential along the Xianshuihe Fault, China. *Journal of Geophysical Research: Solid Earth*, *126*, e2020JB021406. https://doi.org/10.1029/2020jb021406

Li, Y., Nocquet, J.-M., Shan, X., & Song, X. (2021). Geodetic observations of shallow creep on the LaohushanHaiyuan fault, Northeastern Tibet. *Journal of Geophysical Research: Solid Earth*, *126*, e2020JB021576. https://doi.org/10.1029/2020jb021576

Li, Y., Shan, X., Qu, C., Liu, Y., & Han, N. (2018). Crustal deformation of the Altyn Tagh fault based on GPS. *Journal of Geophysical Research: Solid Earth*, *123*(11), 10309–10322. https://doi.org/10.1029/2018jb015814

Lienkaemper, J. J., & McFarland, F. S. (2017). Long-term afterslip of the 2004 M 6.0 Parkfield, California, earthquake-Implications for forecasting amount and duration of afterslip on other major creeping faults. *Bulletin of the Seismological Society of America*, *107*(3), 1082–1093. https://doi.org/10.1785/0120160321

Loveless, J. P., & Meade, B. J. (2011). Partitioning of localized and diffuse deformation in the Tibetan Plateau from joint inversions of geologic and geodetic observations. *Earth and Planetary Science Letters*, *303*(1–2), 11–24. https://doi.org/10.1016/j.epsl.2010.12.014

McCaffrey, R., Qamar, A. I., King, R. W., Wells, R., Khazaradze, G., Williams, C. A., et al. (2007). Fault locking, block rotation and crustal deformation in the Pacific Northwest. *Geophysical Journal International*, *169*(3), 1315–1340. https://doi.org/10.1111/j.1365-246x.2007.03371.x

Menke, W. (1989). *Geophysical data analysis: Discrete inverse theory*. San Diego: Academic Press.

Minson, S. E., Simons, M., & Beck, J. L. (2013). Bayesian inversion for finite fault earthquake source models I–Theory and algorithm. *Geophysical Journal International*, *194*(3), 1701–1726. https://doi.org/10.1093/gji/ggt180

Nocquet, J. M. (2018). Stochastic static fault slip inversion from geodetic data with non-negativity and bound constraints. *Geophysical Journal International*, *214*(1), 366–385. https://doi.org/10.1093/gji/ggy146

Nocquet, J. M., Jarrin, P., Vallée, M., Mothes, P. A., Grandin, R., Rolandone, F., et al. (2017). Supercycle at the Ecuadorian subduction zone revealed after the 2016 Pedernales earthquake. *Nature Geoscience*, *10*(2), 145–149. https://doi.org/10.1038/ngeo2864

Ozener, H., Dogru, A., & Turgut, B. (2013). Quantifying aseismic creep on the Ismetpasa segment of the North Anatolian Fault Zone (Turkey) by 6 years of GPS observations. *Journal of Geodynamics*, *67*, 72–77. https://doi.org/10.1016/j.jog.2012.08.002

Papadimitriou, E., Wen, X., Karakostas, V., & Jin, X. (2004). Earthquake triggering along the Xianshuihe fault zone of western Sichuan, China. *Pure and Applied Geophysics*, *161*(8), 1683–1707. https://doi.org/10.1007/s00024-003-2471-4

Patil, A., Huard, D., & Fonnesbeck, C. J. (2010). PyMC: Bayesian stochastic modelling in Python. *Journal of Statistical Software*, *35*(4), 1–81. https://doi.org/10.18637/jss.v035.i04

Qiao, X., & Zhou, Y. (2021). Geodetic imaging of shallow creep along the Xianshuihe fault and its frictional properties. *Earth and Planetary Science Letters*, *567*(2021), 117001. https://doi.org/10.1016/j.epsl.2021.117001

Ran, Y., Chen, L., Cheng, J., & Gong, H. (2008). Late Quaternary surface deformation and rupture behavior of strong earthquake on the segment north of Mianning of the Anninghe fault. *Science in China, Series D: Earth Sciences*, *51*(9), 1224–1237. https://doi.org/10.1007/s11430-008-0104-6

Rousset, B., Jolivet, R., Simons, M., Lasserre, C., Riel, B., Milillo, P., et al. (2016). An aseismic slip transient on the North Anatolian Fault. *Geophysical Research Letters*, *43*, 3254–3262. https://doi.org/10.1002/2016gl068250

Rui, X., & Stamps, D. S. (2016). Present-day kinematics of the eastern Tibetan Plateau and Sichuan Basin: Implications for lower crustal rheology. *Journal of Geophysical Research: Solid Earth*, *121*(5), 3846–3866. https://doi.org/10.1002/2016jb012839

Segall, P. (2010). *Earthquake and volcano deformation*. Princeton, NJ: Princeton University Press.

Shan, B., Xiong, X., Zheng, Y., Jin, B., Liu, C., Xie, Z., & Hsu, H. (2013). Stress changes on major faults caused by 2013 Lushan earthquake and its relationship with 2008 Wenchuan earthquake. *Science in China, Series D: Earth Sciences*, *56*(7), 1169–1176. https://doi.org/10.1007/s11430-013-4642-1

Shen, Z. K., Lü, J., Wang, M., & Bürgmann, R. (2005). Contemporary crustal deformation around the southeast borderland of the Tibetan Plateau. *Journal of Geophysical Research*, *110*, B11409. https://doi.org/10.1029/2004jb003421

Sieh, K., Natawidjaja, D. H., Meltzner, A. J., Shen, C. C., Cheng, H., Li, K. S., et al. (2008). Earthquake supercycles inferred from sea-level changes recorded in the corals of west Sumatra. *Science*, *322*(5908), 1674–1678. https://doi.org/10.1126/science.1163589

Stevens, V. L., & Avouac, J. P. (2015). Interseismic coupling on the main Himalayan thrust. *Geophysical Research Letters*, *42*(14), 5828–5837. https://doi.org/10.1002/2015gl064845

Sun, H., He, H., Ikeda, Y., Wei, Z., Chen, C., Xu, Y., et al. (2019). Paleoearthquake history along the southern segment of the Daliangshan fault zone in the southeastern Tibetan Plateau. *Tectonics*, *38*, 2208–2231. https://doi.org/10.1029/2018tc005009

Tapponnier, P., & Molnar, P. (1977). Active faulting and tectonics in China. *Journal of Geophysical Research*, *82*(20), 2905–2930. https://doi.org/10.1029/jb082i020p02905

Tapponnier, P., Zhiqin, X., Roger, F., Meyer, B., Arnaud, N., Wittlinger, G., & Yang, J. (2001). Oblique stepwise rise and growth of the Tibet Plateau. *Science*, *294*(5547), 1671–1677. https://doi.org/10.1126/science.105978

Thompson, T. B., Plesch, A., Shaw, J. H., & Meade, B. J. (2015). Rapid slip-deficit rates at the eastern margin of the Tibetan plateau prior to the 2008 Mw 7.9 Wenchuan earthquake. *Geophysical Research Letters*, *42*(6), 1677–1684. https://doi.org/10.1002/2014gl062833

Wang, H., Wright, T. J., & Biggs, J. (2009). Interseismic slip rate of the northwestern Xianshuihe fault from InSAR data. *Geophysical Research Letters*, *36*, L03302. https://doi.org/10.1029/2008gl036560

Wang, W., Qiao, X., Yang, S., & Wang, D. (2017). Present-day velocity field and block kinematics of Tibetan Plateau from GPS measurements. *Geophysical Journal International*, *208*(2), 1088–1102. https://doi.org/10.1093/gji/ggw445

Wang, Y., Wang, E., Shen, Z., Wang, M., Gan, W., Qiao, X., et al. (2008). GPS-constrained inversion of present-day slip rates along major faults of the Sichuan-Yunnan region. *Science in China, Series D: Earth Sciences*, *51*(9), 1267–1283. https://doi.org/10.1007/s11430-008-0106-4

Wang, Y., Wang, M., & Shen, Z.-K. (2017). Block-like versus distributed crustal deformation around northeastern Tibetan Plateau. *Journal of Asian Earth Sciences*, *140*, 31–47. https://doi.org/10.1016/j.jseaes.2017.02.040

Weertman, J., & Weertman, J. R. (1964). *Elementary dislocation theory* (p. 213). New York: MacMillan.

Wei, M., Sandwell, D., & Smith-Konter, B. (2010). Optimal combination of InSAR and GPS for measuring interseismic crustal deformation. *Advances in Space Research*, *46*(2), 236–249. https://doi.org/10.1016/j.asr.2010.03.013

Wells, D. L., & Coppersmith, K. J. (1994). New empirical relationships among magnitude, rupture length, rupture width, rupture area, and surface displacement. *Bulletin of the Seismological Society of America*, *84*(4), 974–1002.

Wen, X., Fan, J., Yi, G., Deng, Y., & Long, F. (2008). A seismic gap on the Anninghe fault in western Sichuan, China. *Science in China, Series D: Earth Sciences*, *51*(10), 1375–1387. https://doi.org/10.1007/s11430-008-0114-4

Wen, X., Ma, S., Xu, X., & He, Y. (2008). Historical pattern and behavior of earthquake ruptures along the eastern boundary of the Sichuan-Yunnan faulted-block, southwestern China. *Physics of the Earth and Planetary Interiors*, *168*(1–2), 16–36. https://doi.org/10.1016/j.pepi.2008.04.013

Wessel, P., Smith, W. H., Scharroo, R., Luis, J., & Wobbe, F. (2013). Generic Mapping Tools: Improved version released. *Eos Transactions AGU*, *94*(45), 409–410. https://doi.org/10.1002/2013eo450001

Yan, B., & Lin, A. (2017). Holocene activity and paleoseismicity of the Selaha Fault, southeastern segment of the strike-slip Xianshuihe Fault Zone, Tibetan Plateau. *Tectonophysics*, *694*, 302–318. https://doi.org/10.1016/j.tecto.2016.11.014

Zhang, J., Wen, X. Z., Cao, J. L., Yan, W., Yang, Y. L., & Su, Q. (2018). Surface creep and slip-behavior segmentation along the northwestern Xianshuihe fault zone of southwestern China determined from decades of fault-crossing short-baseline and short-level surveys. *Tectonophysics*, *722*, 356–372. https://doi.org/10.1016/j.tecto.2017.11.002

Zhang, L., Cao, D., Zhang, J., & Sui, L. (2018). Interseismic fault movement of Xianshuihe Fault Zone based on across-fault deformation data and InSAR. *Pure and Applied Geophysics*, *176*(2), 649–667. https://doi.org/10.1007/s00024-018-1989-4

Zhang, Z., McCaffrey, R., & Zhang, P. (2013). Relative motion across the eastern Tibetan Plateau: Contributions from faulting, internal strain and rotation rates. *Tectonophysics*, *584*, 240–256. https://doi.org/10.1016/j.tecto.2012.08.006

Zhao, D., Qu, C., Shan, X., Gong, W., Zhang, Y., & Zhang, G. (2018). InSAR and GPS derived coseismic deformation and fault model of the 2017 Ms7.0 Jiuzhaigou earthquake in the Northeast Bayanhar block. *Tectonophysics*, *726*, 86–99. https://doi.org/10.1016/j.tecto.2018.01.026

Zheng, G., Wang, H., Wright, T. J., Lou, Y., Zhang, R., Zhang, W., et al. (2017). Crustal deformation in the India-Eurasia collision zone from 25 years of GPS measurements. *Journal of Geophysical Research: Solid Earth*, *122*(11), 9290–9312. https://doi.org/10.1002/2017jb014465